Hindawi
International Journal of Aerospace Engineering
Volume 2021, Article ID 5128136, 18 pages
https://doi.org/10.1155/2021/5128136

Research Article

Power Fan Design of Blended-Wing-Body Aircraft with Distributed Propulsion System

Yuan Jia, Jinye Li, and Jianghao Wu

School of Transportation Science and Engineering, Beihang University, 37 Xueyuan Rd. Haidian District, Beijing 100191, China

Correspondence should be addressed to Jianghao Wu; buaawjh@buaa.edu.cn

Received 22 May 2021; Revised 27 July 2021; Accepted 11 August 2021; Published 8 September 2021

Academic Editor: Giovanni Delibra

A blended-wing-body aircraft has the advantages of high lift-to-drag ratio, low noise, and high economy compared with traditional aircraft. It is currently a solution with great potential to become a future civilian passenger aircraft. However, most airplanes with this layout use distributed power, and the power system is on the back of the fuselage, with embedded or back-supported engines. This type of design causes the boundary layer suction effect. The boundary layer ingestion (BLI) effect can fill the wake of the aircraft and improve the propulsion efficiency of the engine. However, it causes huge design difficulties, especially when the aircraft and the engine are strongly coupled. In this paper, an aircraft with a coupled engine configuration is studied. The internal and external flow fields are calculated through numerical simulation. A realistic calculation model is obtained through the coupling of boundary conditions. On the basis of the influence of the external flow on the internal flow under the coupled condition, the influence of the BLI effect on the aerodynamic performance of the fan is investigated.

1. Introduction

A blended-wing-body (BWB) aircraft is a highly viable and promising layout for commercial aircraft [1–7]. The high lift-to-drag ratio of BWB aircraft results in small fuel consumptions [8–11]. This condition creates great economic benefits for airlines and meets the basic requirements of green aviation development with its low emissions and low pollution [12]. Boundary layer suction works by sucking low-energy fluid into the back of an aircraft so that the engine uses less energy to produce the same thrust [13]. A power system with boundary layer ingestion (BLI) effect is placed at the back of the fuselage, and its ejected gas fills the fuselage wake, reducing the mixing loss and differential pressure resistance caused by the speed difference; this condition is beneficial to the aircraft as a whole [14–16]. However, the BLI effect seriously increases the intake distortion, affects the pressure ratio and efficiency of the fan, and brings many difficulties to the design of the power fan [17]. This paper investigates the design of the power fan of an airlift-coupled wing-body fusion aircraft with the BLI effect.

For studies concentrating on the performance of fans under deviation, some models, such as parallel pressurizer model and volumetric force model, were used for simplification in previous studies due to the difficulty of directly simulating the deviation and the huge calculation amount of the internal flow field. These models were applied to simplify the calculation while ensuring a certain degree of accuracy. Goldberg et al. [18] developed a method to match propulsion system flow and tube flow to simulate the internal flow field under boundary layer inhalation and validated it with NASA's N3-X model. They found that the inlet distortion affected thrust more remarkably than fan efficiency. Budziszewski et al. [19] used a parallel pressurizer model and Xfoil to design a 2D fan blade pattern. The calculations show that the BLI effect can obtain 2.4% power-saving coefficient efficiency and can save power. On the basis of the volumetric

force model, Guo Jin et al. [20] numerically simulated the intake distortion of a large-bypass-ratio fan/boost stage and provided the following conclusions. The distortion transfer characteristics exhibited at different blade heights of the large-bypass-ratio fan rotor vary greatly and the total pressure distortion at the rotor blade tip is smaller than that at the blade root. Fidalgo et al. [21] studied the interaction between circumferential total pressure inlet distortion and a single-stage transonic axial fan, NASA Stage 67, by using the experimentally validated full-loop 3D nonconstant Reynolds-averaged Navier–Stokes (RANS) technique. The results show that the total pressure distortion causes uneven static pressure distribution and significant circumferential and radial airflow angles in areas with small rotor inlet radii. The induced circumferential airflow seriously influences the work capacity of the entire rotor channel and causes the total pressure distortion to be transmitted to the entire rotor flow path.

In this paper, a realistic computational model of the coupling with boundary conditions is investigated for coupled BWB aircraft. The effect of external flow on internal flow in the coupled case and the effect of the BLI effect on the aerodynamic performance of the fan are explored.

2. Models and Methods

2.1. Models. The outflow object studied in this paper is a distributed power BWB-350 aircraft model and the design parameters are shown in Table 1.

The BWB-350 uses a powertrain of two turboshaft engines as power generators, driving seven power fans to provide thrust. The 3D model of the outflow part of the powertrain consists mainly of the fairing, S-shaped inlet, and nozzle, with the inlet and outlet boundaries of the outflow placed in front and behind the power fans to realistically simulate the boundary layer inflow into the fan area. The power system is arranged with the two turboshaft engines in the middle, and the power fans are evenly arranged at the rear of the fuselage center. In this paper, the outflow powertrain inlet and outlet areas; initial spread length; longitudinal length and aerodynamic shape of the BWB aircraft, initial inlet, and outlet boundary conditions; and flow rates are based on the BWB-350 scheme, which is partially designed by the group. The initial design parameters of BWB-350 and power system are shown in Table 2.

The internal flow of the electric propulsion-powered fan used in the abovementioned BWB aircraft is investigated. This aircraft is powered by a turboshaft engine, with an inlet duct, a primary fan (including rotor and stators), and a rectangular tail nozzle design. The design parameters of the distributed power system are shown in Table 3.

The power system is mounted on the aircraft in a semiembedded manner, and the external fairing shape is a low-drag wing type. Its inlet in the outflow section is a rectangle with the same total area as the nine engine inlets, as shown in the fairing in Figure 1, to simplify the equivalent. The two cores and the seven power fans inside the fairing are shown in Figure 1, with a 2D illustration of the power fan interior shown in the plan view to the right.

Table 1: Overall design parameters of BWB-350.

Overall parameter	BWB-350
Cruise altitude (m)	11000
Cruise Mach number (Ma)	0.85
Gliding speed (m/s)	72
Maximum takeoff weight (kg)	230000
Cruise lift-to-drag ratio (K)	23

Table 2: Initial parameters list of BWB-350 and power system.

Design parameters	Design values
Fuselage length (m)	44.6
Spread length (m)	68.2
Reference total area (m^2)	560
Average aerodynamic chord length (m)	10.2
Engine section length (m)	5.88
Inlet location from leading edge (m)	35.6
Inlet area (m^2)	18.53
Tail nozzle outlet area (m^2)	14.68

Table 3: Distributed power system parameters of BWB-350.

Overall parameters	
Axial length of fan section (m)	1.08
Maximum outer diameter of engine (m)	1.964
Inner diameter of engine (m)	0.9
Number of fan stages	1
Rotor–stator ratio	1 : 2

The two cores are ignored because this paper focuses on the power fan section. The 3D structure inside the power fan is shown in Figure 2. It mainly consists of the inlet, the primary fan (including the stators and rotors), and the constricted tail nozzle.

The paper fan leaf type is established according to literature [22], and the 3D leaf Shan channel is developed on the basis of the leaf type. The blade geometry parameters are shown in Table 4.

2.2. Methods. The commercial software Fluent is used for the internal and external flow field calculations in this paper. For the external flow part, the 3D constant RANS is used as the control equation, and the second-order accuracy solution based on an implicit coupled pressure solver is selected. For the external flow, considering that the cruise Mach number of the BWB-350 is 0.85, the Spalart–Allmaras (S–A) model is adopted because it is more accurate than other turbulence models in solving the airfoil aerodynamic

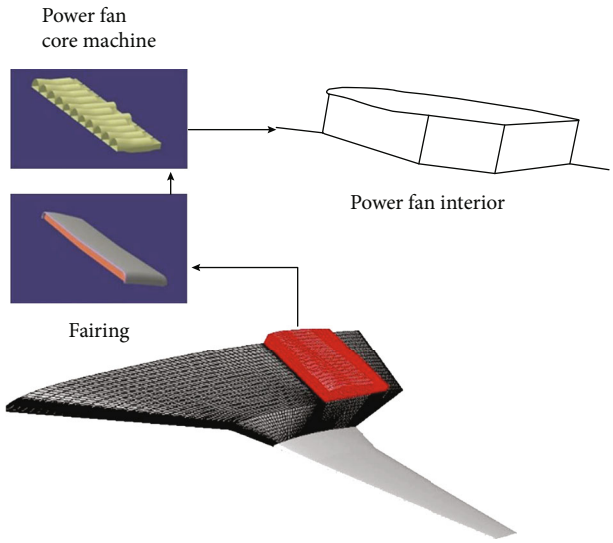

Figure 1: Diagram of inner outflow model.

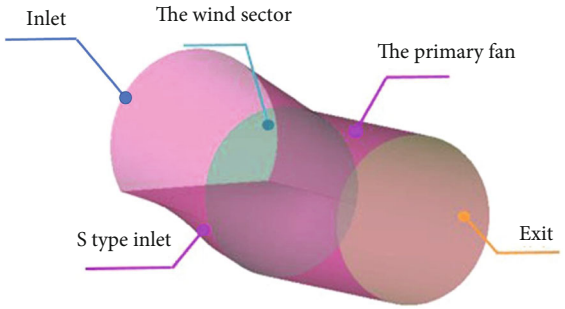

Figure 2: Power fan model.

Table 4: Blade geometry design.

Overall parameters	Design values
Blade chord length (m)	0.1273
Leading edge radius (m)	0.00114
Trailing edge radius (m)	0.00157
Installation angle (°)	14.2
Trailing angle (°)	14.4
Grid distance (m)	0.254

parameters in the subsonic flow field. Also, the solving processes are targeted at optimizing the airfoil, so it is also more accurate for capturing the separation and transition of the outflow airfoil. In addition, as an equation model, it consumes fewer computing resources and converges faster. This is also why S–A model is widely used in reasons in the aviation sector. The object surface uses a no-slip boundary condition. The engine inlet boundary condition is the pressure outlet, and the tailpipe outlet boundary condition is the mass flow inlet.

Table 5: Verification of the first layer grid height of 3D outflow field.

Grid density (million)	Height of first grid layer	C_L	C_D	K
3.0	3.00E−04	0.310745	0.014405	21.572
3.0	1.00E−04	0.311045	0.014417	21.575
3.0	5.00E−05	0.314045	0.014437	21.752
3.0	3.00E−05	0.314682	0.014438	21.795

Table 6: Verification of grid density of 3D outflow field.

Grid density (million)	Height of first grid layer	C_L	C_D	K
1.0	5.00E−05	0.304928	0.015642	19.497
2.0	5.00E−05	0.312245	0.014854	21.021
3.3	5.00E−05	0.314682	0.014437	21.797
4.3	5.00E−05	0.314945	0.014237	21.917

For the internal flow section, a single-channel model is used to simulate the entire flow field numerically by means of periodic boundaries. The k-epsilon turbulence model is used although the k-omega or SST model is shown in the literature to be more accurate for the wall separation and transition capture of the internal flow, the k-epsilon turbulence model is used in the actual calculations because it is best to converge, and the other two turbulence models have non-convergence. A 3D double accuracy, pressure implicitly coupled constant solver, scalable wall functions, and energy equations in second-order windward format are utilized.

2.3. Method Validation

2.3.1. External Flow Field. In this paper, only the longitudinal aerodynamic parameters are analyzed. Considering the computational cost, only the half mode of the aircraft is calculated numerically with a C-H structural grid. The fuselage length of 40 times is chosen for the far-field chordal direction. As it can be seen from Tables 5 and 6, at a grid height of 5.00E−05 and a grid density of 3.3 million, the lift coefficient C_L and drag coefficient C_D of the aircraft tend to be stable. Therefore, the grid with a density of 3.3 million and a first grid height of 5.00E−05 is used for subsequent calculations.

2.3.2. Internal Flow Field. The same 3D model is built from the data given in literature [23], and the corresponding computational grid is created. The grid is shown in Figure 3.

The calculation grid of the internal flow field used in this paper is verified, and the specific values are shown in Tables 7 and 8. The total pressure of the inlet and outlet increases first and then decreases, and the flow rate does not change with the decrease in grid height. Considering the calculation cost and calculation accuracy, the grid with a density of 950,000 and a grid height of 1.00E−05 of the first layer is selected for subsequent calculations.

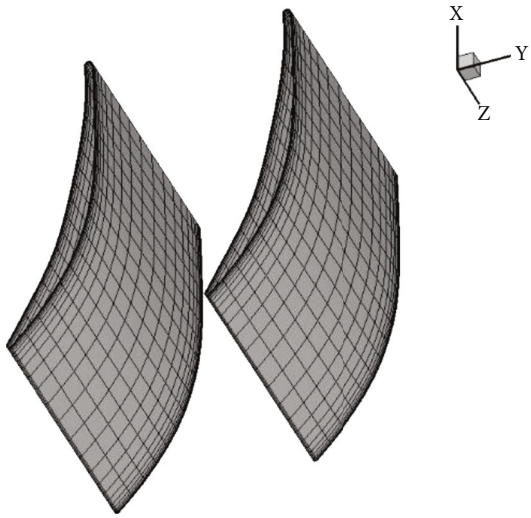

Figure 3: Blade grid partition.

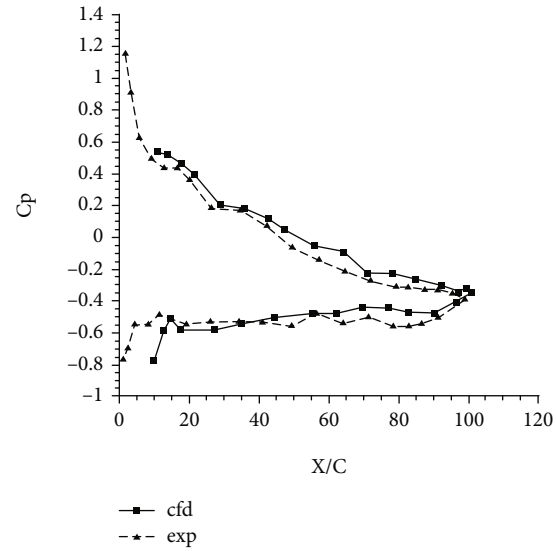

Figure 4: Comparison of pressure coefficients between experimental and numerical results.

Table 7: Verification of the first layer grid height of the 3D internal flow field.

Grid density (million)	Height of first grid layer	Flow rates (kg/s)	Total inlet pressure (Pa)	Total outlet pressure (Pa)
0.95	5.00E−04	4.3	4902	5066
0.95	2.00E−05	4.3	5037	5221
0.95	1.00E−05	4.3	5152	5184
0.95	5.00E−06	4.3	5088	5209

Table 8: Grid density verification of 3D internal flow field.

Grid density (million)	Height of first grid layer	Flow rates (kg/s)	Total inlet pressure (Pa)	Total outlet pressure (Pa)
0.70	1.00E−05	4.2	4928	5078
0.95	1.00E−05	4.3	5152	5184
1.20	1.00E−05	4.3	5069	5200

After verifying the irrelevance of the grid, the pressure coefficient data of the pressure surface and suction surface are intercepted from the results of the verification calculation example at the position of 50% blade height. The comparison with those obtained through Cascade's blowing experiment in the literature is shown in Figures 4 and 5.

The pressure coefficients on the pressure and suction surfaces correspond well to the data in the literature under the same calculation conditions as the experiments, with a maximum error of less than 6%. The experimental and numerical calculations show essentially the same trend in the pressure coefficients with chord length. The reason why the suction surface at the leading edge has a difference with the experimental results is that the geometry of the intercepted data is slightly different but is the same as the experimental data in the trend. Therefore, the results of the grid using the above design method can be considered accurate and reliable.

3. Coupling Model and Verification

3.1. Internal and Outflow Iterative Method. In the traditional design, the aircraft and the engine are designed separately. This condition causes inconsistent calculation conditions when they are assembled after the design. This paper studies the establishment of the internal and external flow coupling model to obtain a design model that is close to the physically realistic calculation conditions and to obtain an integrated flight and engine design model. Therefore, simulating the distribution of the airflow from the back of the aircraft into the fan inlet at high altitude cruise conditions and the aerodynamic parameters on the boundary between the powertrain and engine sections of the aircraft under these inlet conditions is necessary to obtain a computational model that facilitates the codesign of the aircraft engine. Most previous studies used a 1D model or the equivalent of the parallel compressor principle to calculate the aerodynamic data for the inlet flow. In this paper, a direct 3D modeling of the fan blades and a 3D numerical simulation are adopted. The grid verification calculation conditions are shown in Table 9.

Figure 6 shows the 3D model of the internal flow fan blade and the grid division. A single-channel model with a periodic boundary is used to simulate the full circumference, and a periodic interface condition is utilized to connect the rotor part and the static subpart grid. The grid division on the connection surface is the same, so as to ensure the accuracy of data transfer.

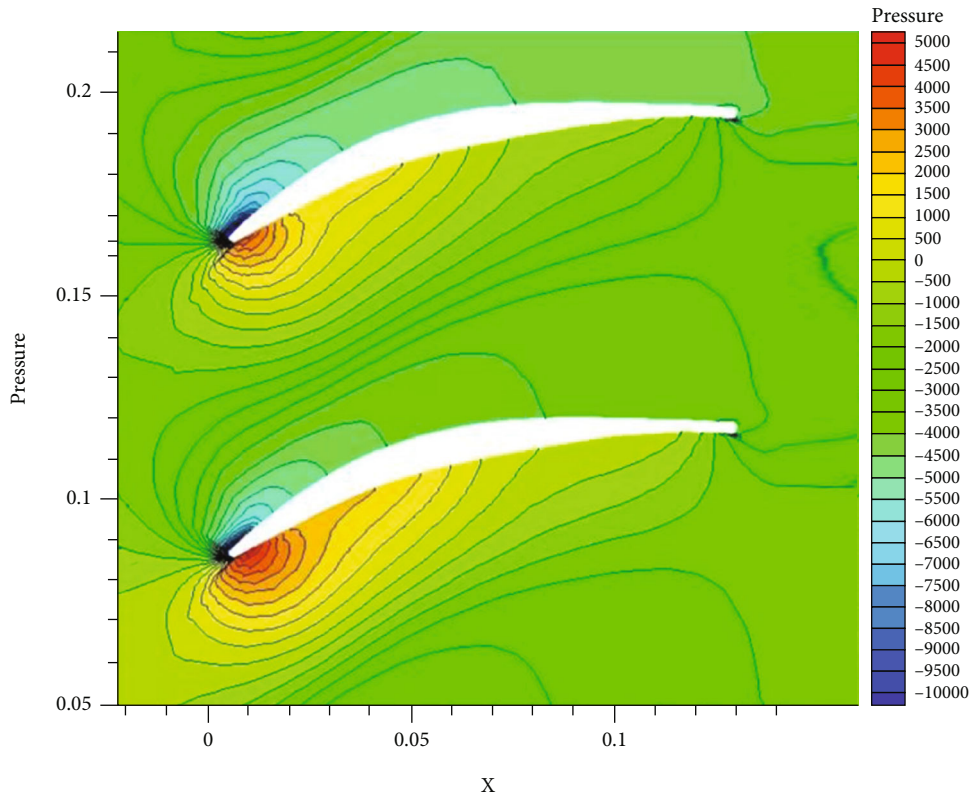

Figure 5: Pressure distribution.

Table 9: Internal flow grid verification calculation conditions.

Overall parameters	Design values
Total inlet temperature (K)	294
Total inlet pressure (Pa)	104365
Inlet Mach number (Ma)	0.25
Static outlet pressure (Pa)	101325
Reynolds number	700000

The velocity inlet is used to define the inlet boundary condition for the internal flow, and Figure 7 shows the velocity distribution for this inlet condition.

For the outflow calculations, the same model of BWB aircraft with distributed propulsion system is used, and the relevant calculations for its longitudinal aerodynamic characteristics are conducted. The main results are shown in Table 10.

Considering the advantages and disadvantages of computational cost and convergence, a cruising angle of attack of 3° is adopted as the final angle of attack for the subsequent coupling with the internal flow.

Finding the boundary conditions where the total pressure and temperature and flow rate are consistent in the numerical calculation of internal and external flows is necessary. MATLAB is used to automatically iterate over the calculated flow field and output results. Fluent is utilized to solve the internal and external flow fields to achieve the

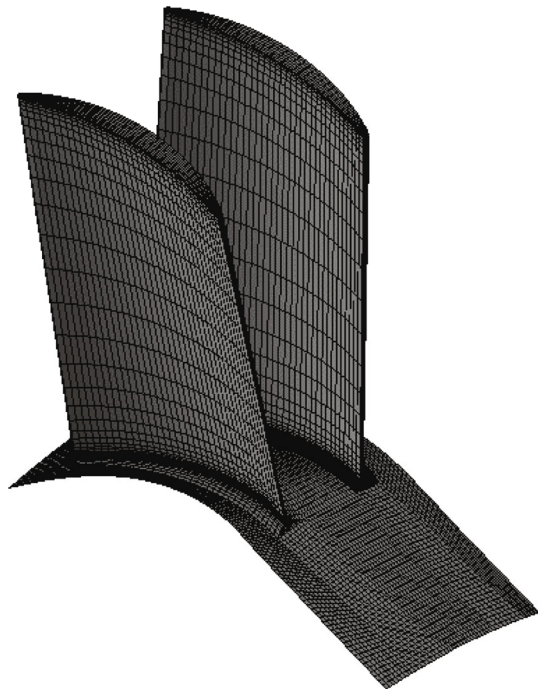

Figure 6: Three-dimensional model and grid of first-order stator.

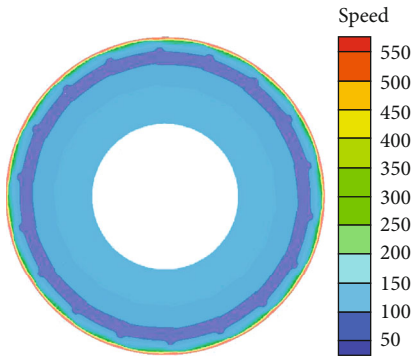

Figure 7: Inlet velocity distribution under pressure inlet condition.

Table 10: Calculation results of the longitudinal characteristics of outflow flow field.

α	C_L	C_D	C_m	K
0	−0.1442	0.0155	0.0448	−9.30323
3	0.3618	0.0160	0.0050	22.5949
5	0.7175	0.0373	−0.0345	19.2359
7	0.9000	0.0802	−0.0346	11.2220
10	0.9500	0.1600	0.0100	5.9375

Note: α is the angle of attack. C_L is the lift coefficient. C_D is the drag coefficient. C_m is the moment coefficient. K is the lift-to-drag ratio.

purpose of iterating over the boundary conditions. The iterative process is shown in Figure 8.

Figure 9(a) shows the inlet and outlet boundaries of the aircraft's powertrain. The A-A′ boundary is the exit section of the inlet tract, where the fan is located, and the B-B′ section is behind the fan section, which is the exit boundary of the outflow powertrain. As shown in Figure 9(b), the C-C′ section is the inlet boundary of the internal flow, and the D-D′ section in front of the tailpipe is the outlet boundary.

The internal and external flow fields are calculated separately due to the difference in scale size. The internal and external flow boundaries shown in Figure 9 are the boundary conditions that need to be iterated. The aerodynamic data of the A-A′ section and the C-C′ section need to be consistent. The aerodynamic data of B-B′ and D-D′ are consistent, which is regarded as the completion of the iteration.

3.2. Coupled Model Iteration Results. With the change in intake airflow, the aerodynamic data of outflow are shown in Table 11. With the increase in the flow rate at the inlet and outlet boundaries of the outflow, the total pressure at the inlet and outlet increases. The static pressure at the outlet increases first and then decreases after the flow rate reaches 1000 kg/s.

Two typical states, 810 kg/s and 984 kg/s flow states, are selected for analysis. Figures 10(a) and 10(b) show the pressure distribution of the aircraft at different inlet flows. Figures 10(c) and 10(d) show the velocity distribution of the two states.

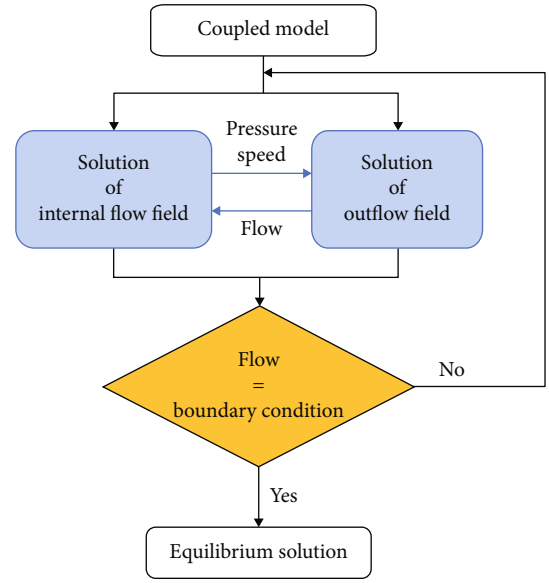

Figure 8: Iterative flowchart of inward and outward flows.

From Figures 10(a) and 10(b), the pressure in front of the inlet is higher at lower flow rates. This condition indicates that the flow rate is smaller compared with the flow capacity, resulting in a blockage at the inlet. As shown in the velocity distribution at the top of the fairing in Figures 10(c) and 10(d), the velocity near the inlet tract is significantly high, indicating a significant overflow. The final iteration of the internal flow converges around this flow rate, as shown in Table 12.

The final result of internal and external couplings is shown in Table 13.

On the basis of the inlet and outlet boundary conditions at the coupling point and the numerical simulation of the outflow field, the lift and drag coefficients are higher than in the previous model designed for outflow only, but the lift-to-drag ratio is lower, as shown in Figure 11.

The temperature of the internal and external flow calculation results is slightly different due to the restriction of boundary conditions. From Table 13, the outlet total pressure, static pressure, and flow rate are similar. The results of internal and external flow total pressure have a difference of 7%. This difference is due to the fact that the outlet Mach number of the external flow field cannot exceed 1. Thus, a certain value of static pressure limits the total pressure, and the difference between internal and external flows in this part is slightly large. The total inlet pressure of the outflow field is a result of the boundary conditions and the forced constraint on the inlet area of the outflow dynamical system. The calculated inlet static pressure value is constant regardless of the flow rate because the inlet area leads to a constant flow rate. Therefore, the calculation of pressure ratio and other data is still subject to the calculation result of internal flow. Under this condition, the two calculations are close to each other and are consistent with the physical state at high altitude.

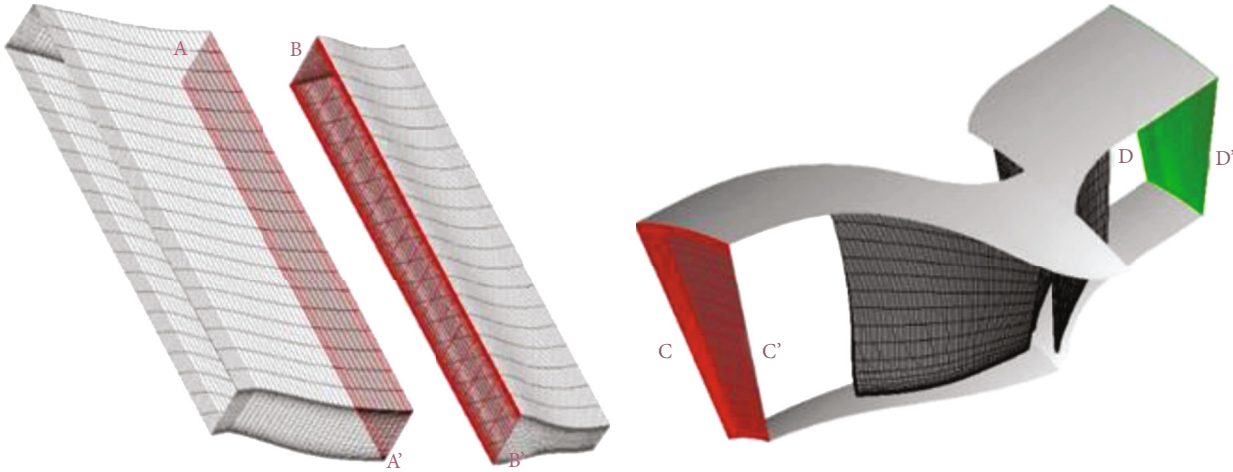

Figure 9: Fan inlet and outlet section diagram. (a) Outflow part of the dynamic system. (b) Internal flow part calculation.

Table 11: Iteration data of 3D outflow field.

Flow rates(kg/s)	Total inlet pressure (Pa)	Total outlet pressure (Pa)	Outlet static pressure (Pa)
810	33,662	49,038	28,698
874	34,072	52,558	29,957
940	34,406	56,697	30,435
984	34,619	59,868	29,904
1002	34,710	61,293	29,501
1023	34,822	63,009	29,093
1134	35,782	71,615	29,095

4. Influence of BLI Effect on the Aerodynamic Performance of Fans

4.1. Comparison with and without BLI Effect. The calculation condition with BLI inlet is the inlet velocity distribution curve calculated using the user-defined function (udf) simulation of the outflow field as described above. The corresponding calculation condition for the unbounded layer inlet is the same total flow rate as with the udf velocity inlet by using an inlet boundary condition with a fixed inlet velocity value. The two calculations are conducted with boundary conditions coupled to the outflow, and the results are compared, as shown in Table 14.

As shown in the data in Table 14, at the operating point of the coupling with the outflow, where the two flows are essentially the same (the inflow flow is the total flow of nine engines), the values of the total inlet pressure with and without the BLI are 50754 and 49389 Pa, respectively. However, the total outlet pressure differs considerably in comparison, with a difference of approximately 6.2% between the two. This condition results in a large difference in the boost ratio, showing that the BLI leads to a reduction in the boost effect. At the same time, the fan efficiency with BLI is also lower than that without BLI. Thus, boundary layer inhalation reduces the pressure ratio and efficiency. The data from three different cross-sectional positions of the rotor blades are intercepted for analysis to analyze the reasons for the reduction. In the position close to the hub, the rotor runner is a constricted runner to intercept the rotor and the stator. Starting at 23% of the dynamic blade height is necessary, which is the first cross-sectional position, followed by 52.4% of the dynamic blade height and 91.26% of the dynamic leaf height. A comparison between the three cross-sections with and without BLI is conducted, as shown in Figure 12.

As shown in Figures 12(a) and 12(b), the BLI leads to backflow during the static lobe pressurization process, where the pressure is low, and overpressurization leads to a localized backflow zone. This condition is caused by the boundary layer intake bringing low energy fluids in the part near the hub, thereby leading to a failure to achieve the design requirements for pressurization. The flow path without BLI flows normally, and the intake distortion does have an effect.

As shown in Figure 12(c), the condition with BLI still produces vortices in the static subpart, affecting the flow quality. The intake distortion affects the entire flow path from the root to the tip of the blade, all with varying degrees of turbulence. As shown in Figure 12(d), no backflow occurs for the situation without BLI in the section closer to the magazine, where the inflow of gas is at a high speed for two conditions.

As shown in Figures 12(e) and 12(f), the cross-section near the hub in the two operating conditions has a chaotic flow field partially because of the constricted flow path, which is essentially near the hub wall in the static subsection and has chaotic vortices. The BLI has the lowest velocity because the incoming flow in this cross-section is all low-energy fluid near the wall. The uniform inlet section has a boundary layer due to the influence of the part of the wall. The boundary layer develops because of the influence of a

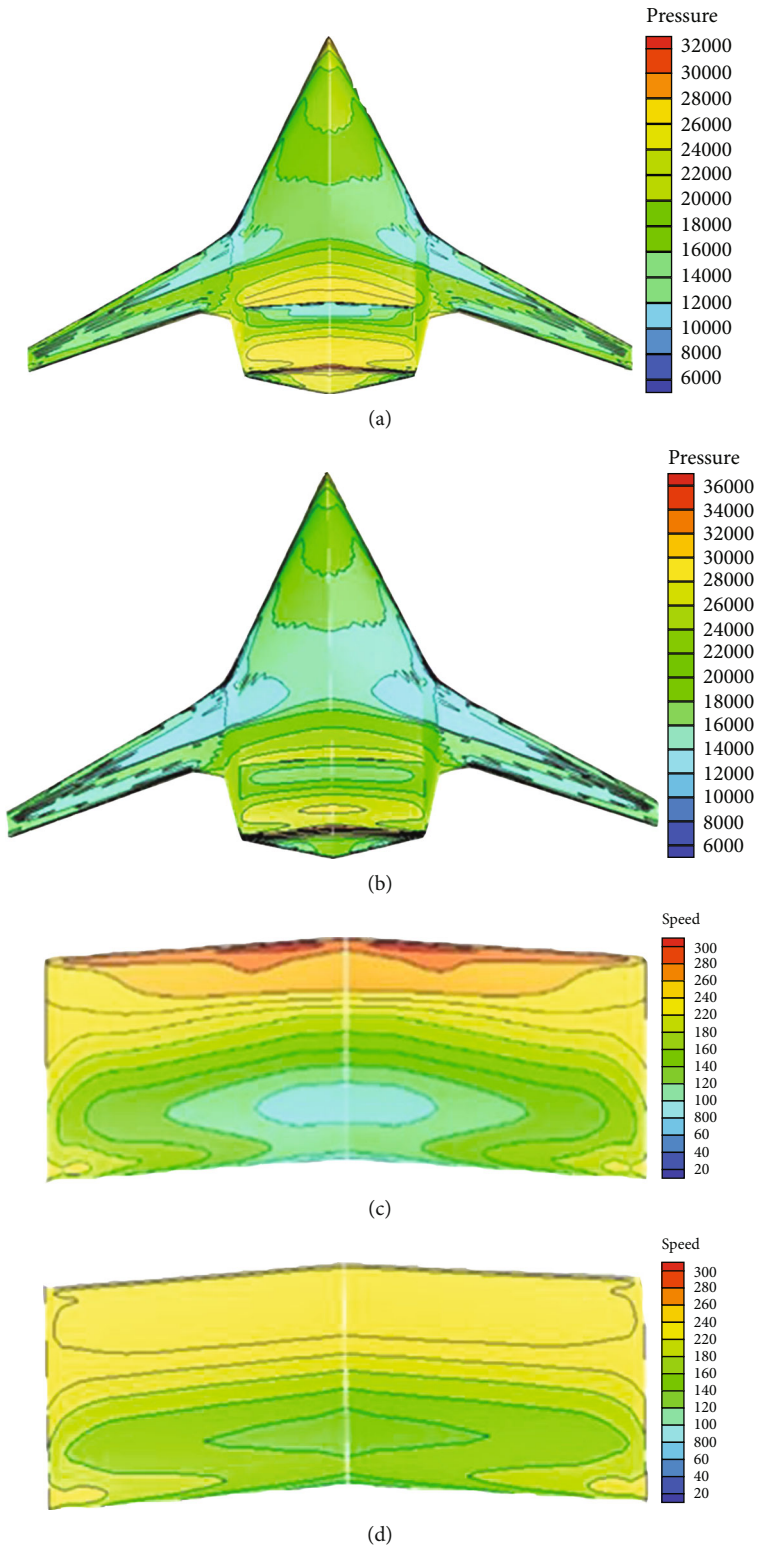

Figure 10: Aircraft pressure nephogram and velocity distribution on the upper surface of power system fairing under different flow rates. (a) The intake flow is 810 kg/s. (b) The intake flow is 984 kg/s. (c) Fairing velocity distribution at 810 kg/s. (d) Fairing velocity distribution at 984 kg/s.

Table 12: Numerical calculation results of 3D internal flow field.

Flow rates (kg/s)	Total inlet pressure (Pa)	Total inlet temperature (K)	Total outlet pressure (Pa)	Total outlet temperature (K)	Outlet static pressure (Pa)
984.9	50,754	265.1	64,478	310	31,700

Table 13: Inner outflow field coupling data.

Parameters	Outflow data	Instream data	Percentage difference
Flow rates (kg/s)	940.0	984.9	4.40%
Total inlet temperature (K)	267.9	265.1	1.04%
Total outlet pressure (Pa)	56,697.0	64,478.0	7.00%
Total outlet temperature (K)	309.0	310.0	0.30%
Outlet static pressure (Pa)	30,435.0	31,700.0	4.00%

part of the wall, thereby creating phenomena, such as backflow and separation that affect the flow quality and aerodynamic performance.

As clearly shown in Figure 13(a), the pressure at the trailing edge of the rotor is significantly higher in the case of without BLI than in the case with BLI. This condition corresponds with the flow diagrams at different blade heights, indicating that the BLI affects the entire flow path and that the flow is extremely chaotic at the 52% blade height position of the rotors. Separation vortices appear in the static subsection, making the boosting effect of the entire primary fan significantly ineffective. A low-pressure zone can be observed in Figure 13(b) at the bottom of the blades and extending upward, indicating that the influence of the low-energy fluid is spreading from the bottom to the top of the blades, affecting the overall fan performance.

4.2. Influence of the Number of Fan Blades. This paper investigates the effect of the number of blades on the performance of the fan under the power system model with BLI effect in the airfoil-body fusion layout, with a total of three blades for numerical calculation: 15, 18, and 24 dynamic blades. The three layouts use the same blade type, mounting angle, and twist angle. The flow rate versus pressure ratio curves is obtained by varying the magnitude of the pressure being applied.

4.2.1. At Sea Level. The performance of the three blade quantities at sea level is first estimated for comparison purposes, and the results of the calculations are shown in Tables 15–17.

The data are plotted. As shown in Figures 14 and 15, the number of blades does not affect the final pressure ratio flow curve, and the effect on efficiency is mainly reflected in whether or not it works near the design point. Different cascade densities have different efficiency curves, which follow essentially the same trend. With the increase in the number of rotor blades, the pressure ratio of 24 rotor blades is higher at lower flow rates. However, the 24 rotor blades do not produce the same pressure ratio as the model with fewer blades at higher flow rates. The fan efficiency of the 15 rotor blades is significantly lower at the same pressure ratio, with a maximum fan efficiency of 83%. The 18 rotor blades reach 86%, and the 24 rotor blades reach around 85%, giving a better overall performance for the 18 rotor blades.

The 15 and 18 rotor blades curves show a similar pressure-flow curve, with some pressure ratio differences at low flow rates. However, they are mostly identical at high flow rates presumably because the difference in the number of blades is small, resulting in a small difference.

From the fan efficiency data, 15 rotor blades are unsuitable, in this design state the efficiency is low, leading to poor pressure ratio and efficiency. The fan efficiency of 18 blades is higher than that of 24 blades. In a comprehensive view, 18 blades are a better solution in the sea level conditions.

The pressure distribution is analyzed, and the pressure distribution clouds for the three models are shown in Figure 16.

As shown in Figure 16, in the case of 15 rotor blades, a low-pressure zone appears in the middle of the blade where the airflow starts to accelerate. In the case of 24 rotor blades, the low-pressure zone appears at the leading edge of the blade where the airflow starts to accelerate from the leading edge. In the case of 18 rotor blades, the low-pressure zone is somewhere in between. This condition is due to the different positions of the airflow inlet angle of attack for different blade numbers with the fixed blade speed.

4.2.2. High-Altitude Cruise State. The number of fan blades does not significantly affect the fan's flow to pressure ratio profile at sea level. However, the focus of this paper is to investigate the performance gap between different rotor blade numbers of the powered fan at high-altitude operating points. Thus, calculations need to be conducted at cruise conditions. The cruising altitude is 11 km, the atmospheric pressure and other gas parameters are changed to this altitude, and the fan model is changed to a 1 : 1 model for calculation. Three rotor blade numbers were used for comparison. All three models used for the high-altitude comparison of different blade numbers are rotor only to remove the effect of different numbers of static subblades.

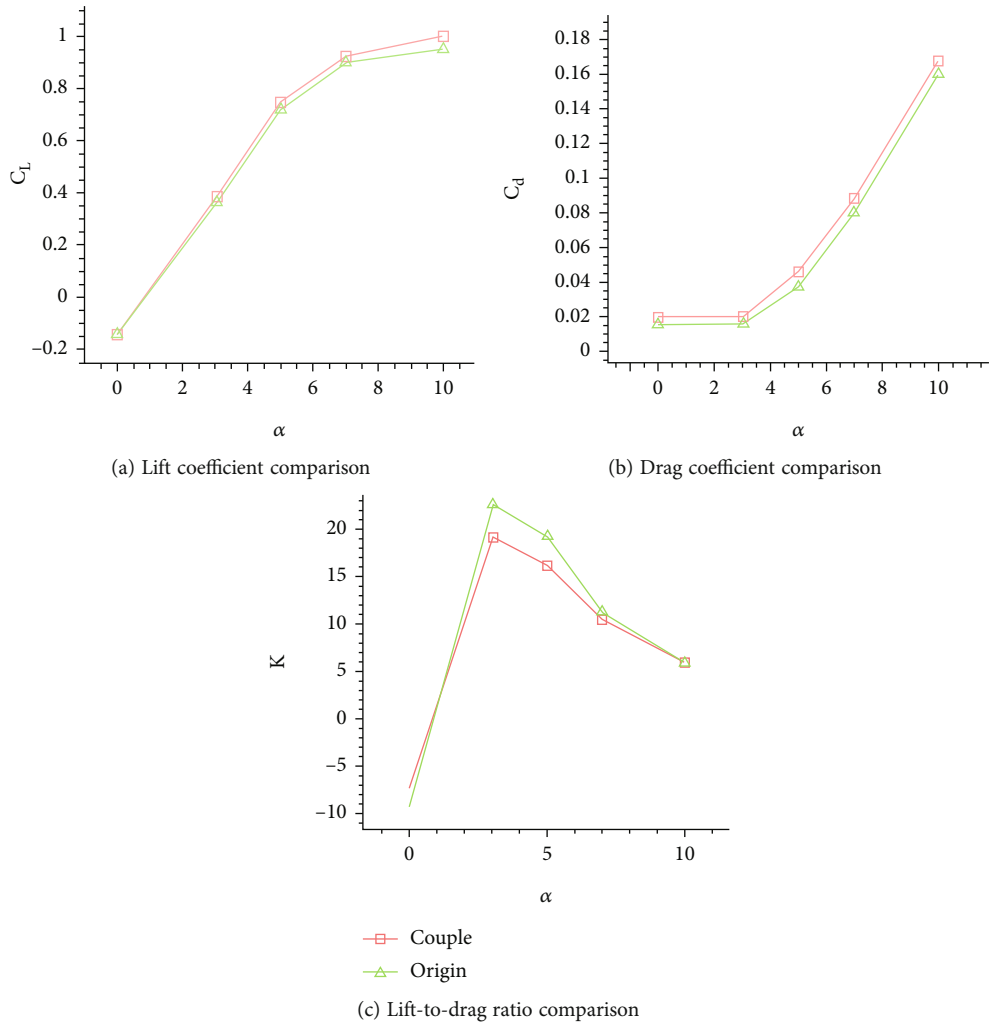

(a) Lift coefficient comparison

(b) Drag coefficient comparison

(c) Lift-to-drag ratio comparison

Figure 11: Calculation results of original boundary conditions and coupling point boundary conditions.

Table 14: Data comparison with and without BLI.

	Flow rates (kg/s)	Total inlet pressure (Pa)	Total outlet pressure (Pa)	Total inlet/outlet temperature (k)	Boost ratio	Fan efficiency
Without BLI	986.0	49,389	68,479	288/329	1.38	65.2%
With BLI	984.9	50,754	64,478	265/310	1.27	43.3%

The inlet conditions were udf files with boundary layer velocity type, simulating the boundary layer inhalation at the back of the fuselage. The above method was used to investigate the effect of rotor blade number on aerodynamic performance at cruise operating point conditions. Only the rotor was used for all blade number comparisons because the number of stators needs to be matched to the rotor. This condition can lead to differences in variables. Some of the calculated data are shown in Tables 18–20.

As shown in the data in Tables 18–20, the model flow rate is greater at cruising altitude and with only the rotor compared with the sea level condition because the air is less dense at cruising altitude and more flow is pumped. The range of pressure ratio variation is greater at high altitude, and the pressure ratio is greater than at sea level although it is still smaller compared with the transformed flow rate from similar criteria. This condition is consistent with the conclusion stated above that a smaller flow rate results in a smaller work mass for propulsion and less thrust. Achieving the thrust required in cruise conditions is difficult.

Figure 17 shows the pressure ratio-flow curves for different blade numbers at high-altitude cruise conditions.

A comparison shows that the pressure ratios at low flow rates are similar for all three blade counts. However, the

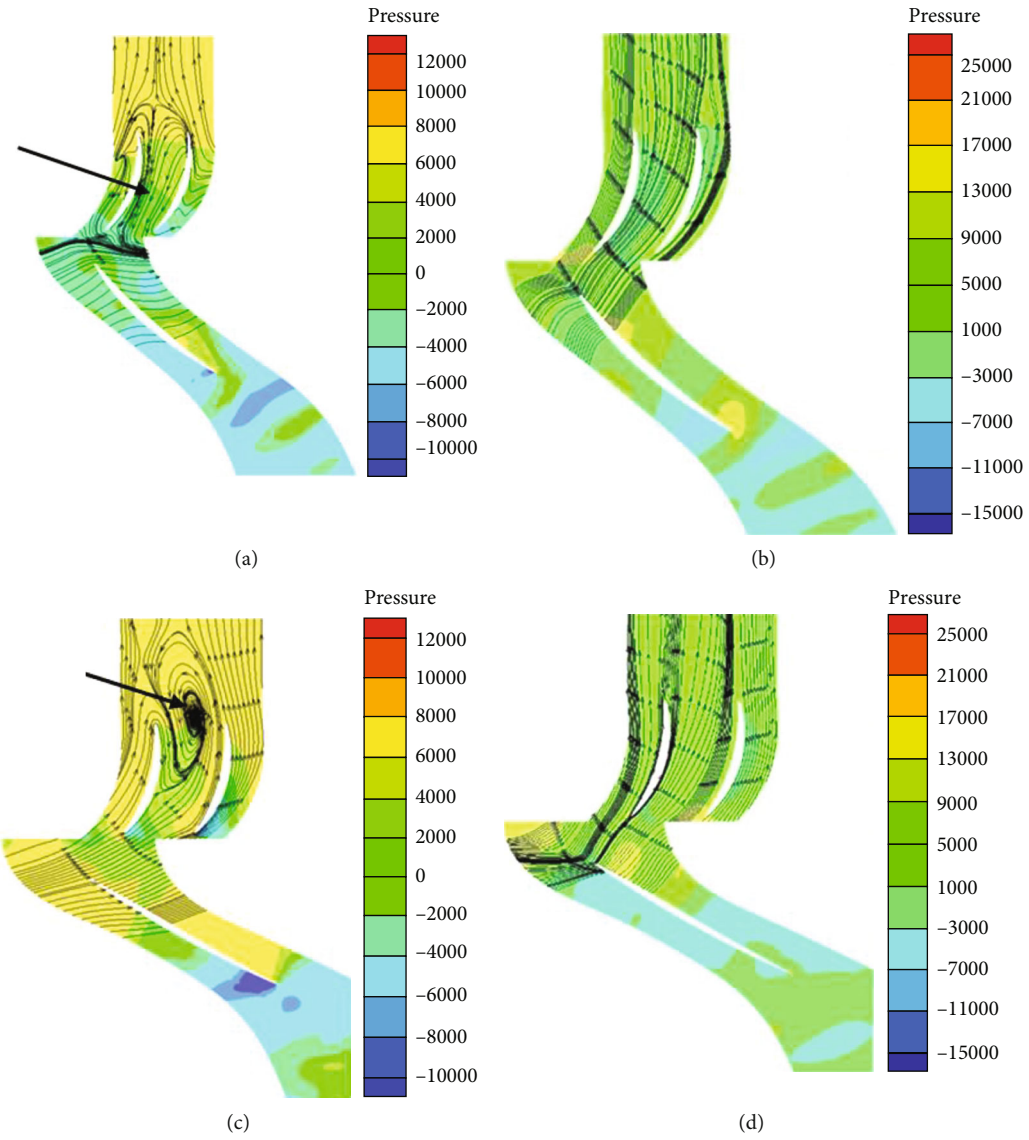

Figure 12: Continued.

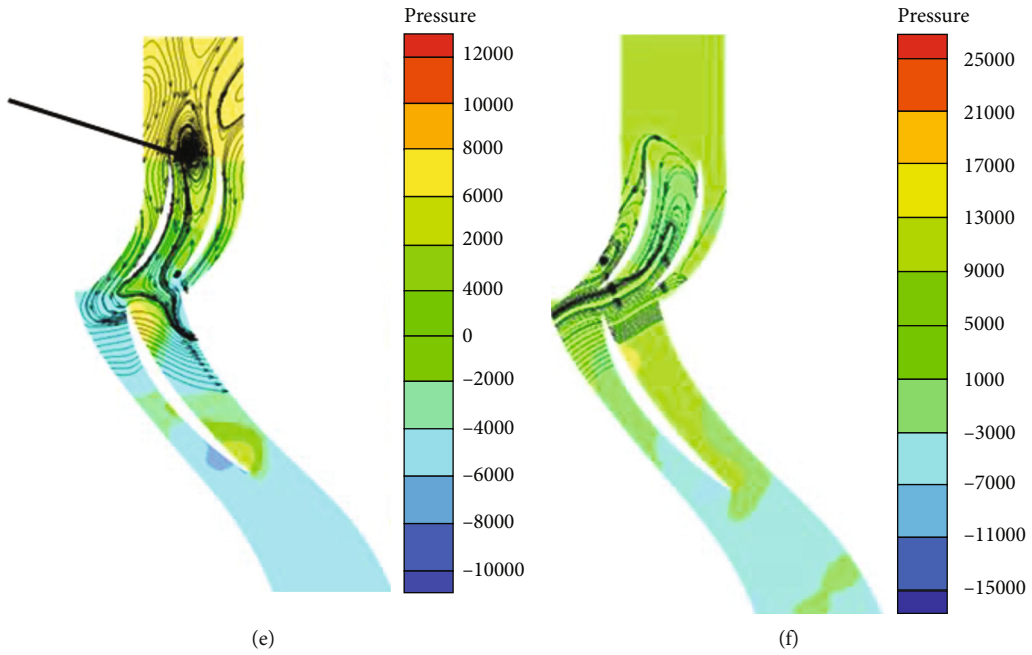

Figure 12: Pressure nephograms with or without BLI at different positions of rotor blade height. (a) Leaf height of 52.4% with BLI. (b) Leaf height of 52.4% without BLI. (c) Leaf height of 91.26% with BLI. (d) Leaf height of 91.26% without BLI. (e) Leaf height of 23.3% with BLI. (f) Leaf height of 23.3% without BLI.

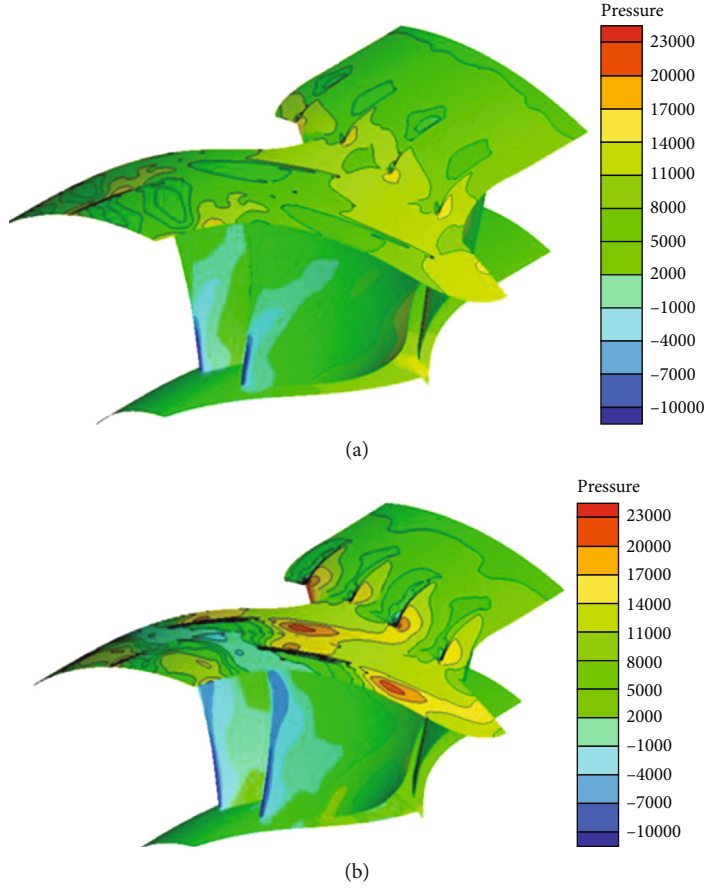

Figure 13: High-altitude pressure nephogram without or with BLI effect. (a) Without BLI. (b) With BLI.

Table 15: Fifteen rotor blades.

Flow rates(kg/s)	Total inlet pressure (Pa)	Total outlet pressure (Pa)	Boost ratio	Fan efficiency
22.15	106,857	138,678	1.297789	0.561094
21.7	106,744	140,981	1.320739	0.788289
21.1	106,944	142,848	1.335727	0.829513
20.8	106,946	143,533	1.342107	0.753364
19.969	106,878	144263	1.349789	0.740856

Table 16: Eighteen rotor blades.

Flow rates(kg/s)	Total inlet pressure (Pa)	Total outlet pressure (Pa)	Boost ratio	Fan efficiency
22.42	107,451	137,974	1.284064	0.867326
22.09	107,639	139,967	1.300342	0.878934
21.71	107,697	142,030	1.318789	0.843172
21.47	107,791	143,026	1.326883	0.822364
21.09	107,847	143,519	1.330765	0.755491
20.36	108,062	145,496	1.337158	0.682653
19.72	108,185	146,125	1.350712	0.646103

Table 17: Twenty-four rotor blades.

Flow rates(kg/s)	Total inlet pressure (Pa)	Total outlet pressure (Pa)	Boost ratio	Fan efficiency
22.05	106,101	137160	1.292730	0.818845
21.71	105927	138204	1.304710	0.823746
21.14	105879	140320	1.325286	0.841195
20.89	105850	141294	1.334849	0.845656
20.50	105,852	143210	1.352924	0.828095
20.27	105910	144224	1.361752	0.766227
19.71	105980	145096	1.369095	0.787453

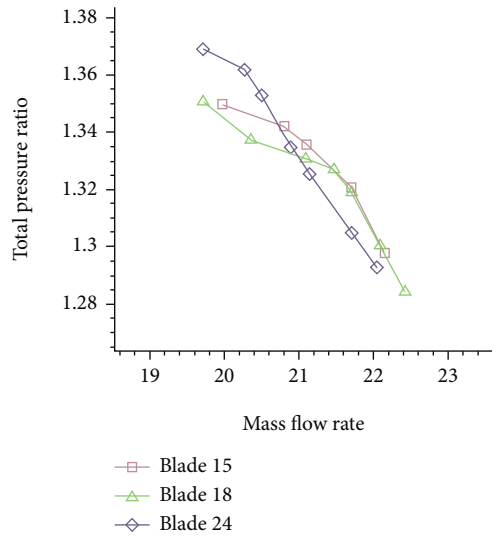

Figure 14: Comparison of the flow-pressure ratio of different blade numbers.

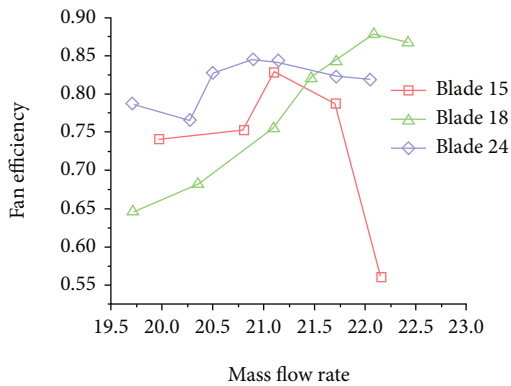

Figure 15: Comparison of the fan efficiency of different blade numbers.

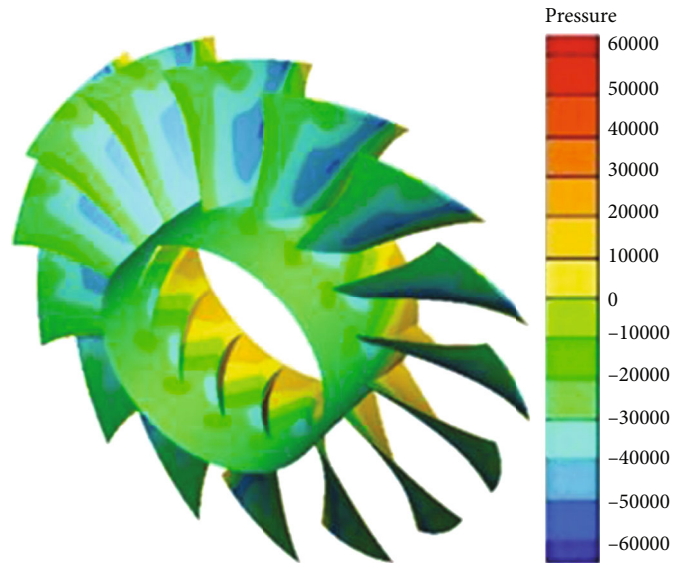

(a)

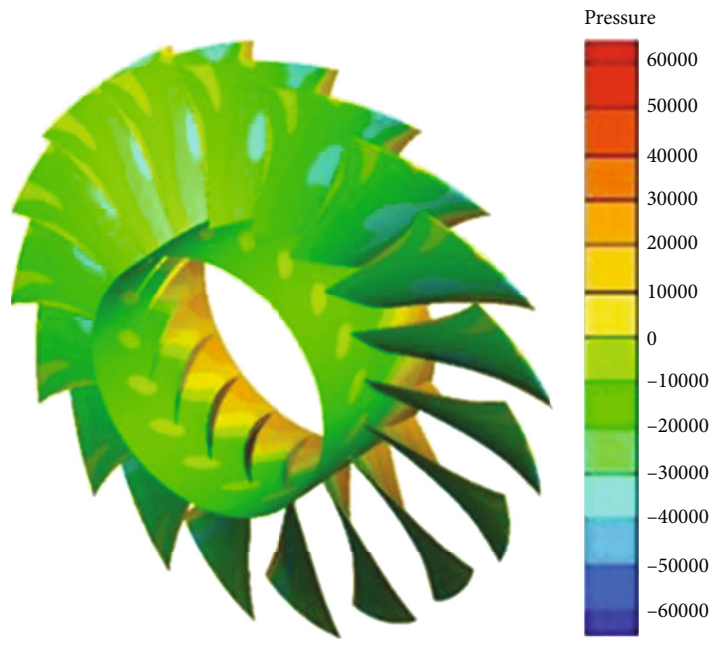

(b)

Figure 16: Continued.

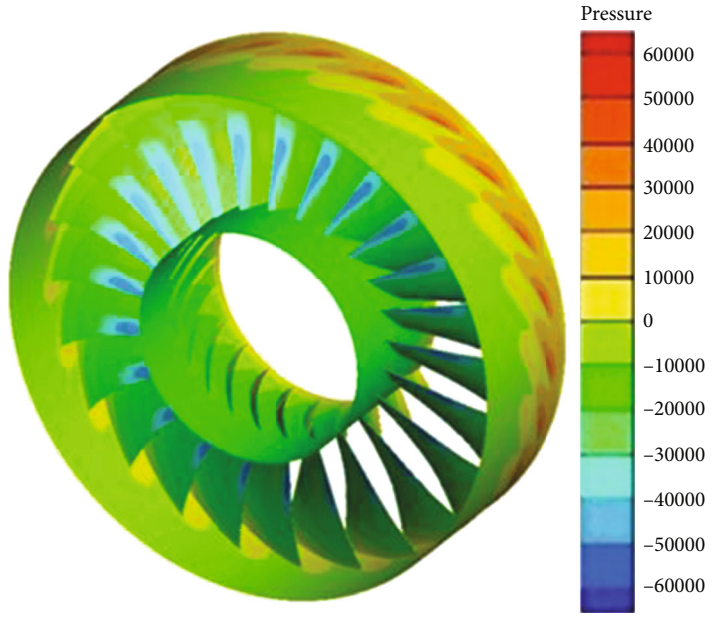

(c)

Figure 16: Pressure cloud images of different blade numbers at sea level. (a) With 15 rotor blades. (b) With 18 blades. (c) With 24 blades.

Table 18: Fifteen rotor blades.

Flow rates (kg/s)	Total inlet pressure (Pa)	Total outlet pressure (Pa)	Boost ratio
52.00	41,149	43,356	1.053634
44.00	41,549	44,456	1.069966
37.70	41,087	50,874	1.238202
31.00	37,955	57,337	1.390657

Table 19: Eighteen rotor blades.

Flow rates (kg/s)	Total inlet pressure (Pa)	Total outlet pressure (Pa)	Boost ratio
56.60	43,577	45,558	1.045460
46.00	43,138	49,001	1.135913
38.10	40,036	52,164	1.302927
32.30	37,246	58,086	1.359523
29.00	37,327	61,208	1.439778
26.70	37,359	62,893	1.493477

model with 24 rotor blades shows a sharp drop in pressure ratio during the flow increase, and the pressure ratio is less than 1 when small pressure is applied. This condition proves that the increase in the number of blades does not improve the pressure boosting capacity at high altitude and diminishes. The changing trend of 15 and 18 rotor blades is not much different. The model with 18 rotor blades performs better than 15 rotor blades in the high flow condition, indicating that at that operating point, 18 blades are a better choice for rotating speed and number of inlet angles.

Table 20: Twenty-four rotor blades.

Flow rates (kg/s)	Total inlet pressure (Pa)	Total outlet pressure (Pa)	Boost ratio
35.22	42,526	43,114	1.013827
31.16	37,507	58,901	1.370400
29.70	37,503	60,837	1.422190
27.00	37,568	62,219	1.456170

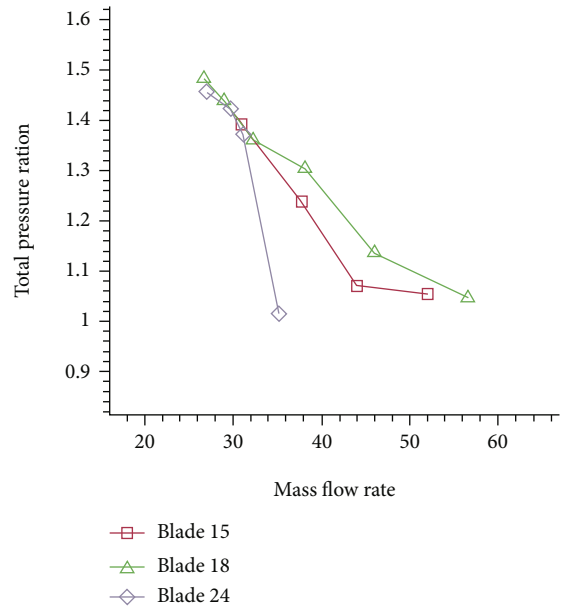

Figure 17: Flow-pressure ratio curve of different blade numbers at high-altitude cruising point.

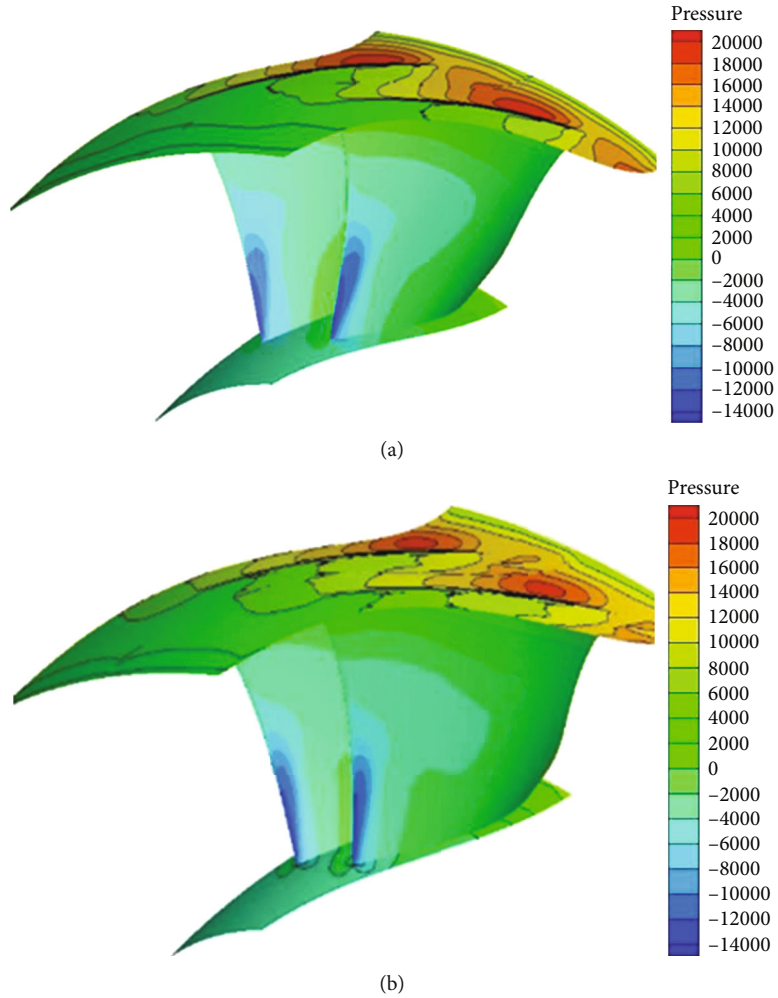

Figure 18: Cloud image of the flow field of different blade numbers at high altitude. (a) With 18 rotor blades. (b) With 24 rotor blades.

The pressure clouds for the 18 and 24 rotor blades (with hub and magazine sections) at the high-altitude cruise point are shown in Figure 18.

With a higher number of blades, the high-pressure area is smaller at the rear of the blades than with 18 rotor blades, indicating that fewer blades have a higher boost ratio for the same intake conditions. As shown in the curves in the graph above, the pressure ratios of the 18 rotor blades are higher than those of the 15 rotor blades at the same flow rate in cruise conditions, which is different from the calculations at sea level. At high altitude and with BLI, the number of blades affects the performance of the power fan to a certain extent, and the speed type of air inlet and the blade twist are related rather than the more or less number of blades. This paper shows that 18 rotor blades are suitable for the current operating conditions.

5. Conclusions

In this paper, a parametric modeling of the aircraft and the power fan blade is conducted on a BWB aircraft with the distributed propulsion system. A grid model of the aircraft and the power fan blade is developed, and the grid independence of the internal and external flows is verified and compared with experimental results. A high-precision, fast-solving numerical calculation method is established for the internal and external flow fields. Numerical simulations of the internal and external flows are conducted at the high-altitude cruise point. Iterations of the power system part of the external flow and the inlet and outlet boundary conditions of the internal flow are performed until the flow rates of the internal and external flows and the total outlet temperature, pressure and static pressure are consistent. This condition is regarded as establishing a coupled model of the internal and external flows at the operating point close to the real physical state. On the basis of the coupled model, the effect of the airflow of the back boundary layer of the power fan on its aerodynamic performance is studied and analyzed. The effect of the louvre density on the fan performance in the presence of the BLI effect is investigated, and the relevant laws are summarized. The following conclusions are drawn.

(1) An iterative method of coupling internal and external flows is designed to obtain an internal and external flow coupling model at the high-altitude cruise

operating point. This method can be used as a reference for future scholars to study internal and external flow models

(2) The coupled equilibrium point of the internal and external flows is given to the inlet conditions where the internal flow field has a boundary layer. The overall performance of the fan is affected mainly by the way the low-energy fluid creates irregular flow in the lower part of the blades and affects the static subpart, with strong separation vortices in the static sub blades by comparing with the uniform inlet model. This condition results in a reduction of the pressurization capacity and backflow in the smaller radius of the fan. Thus, the overall boost ratio of the fan is inferior to that of the fan model without BLI

(3) On the basis of calculations of the equilibrium point of the internal and external flow coupling, different numbers of rotor blades do not significantly affect the flow-pressure ratio performance curve in the calculation of the sea level condition, where the inlet and outlet are pressure conditions

(4) In terms of fan efficiency, 15 blades are less efficient, whereas 18 and 24 rotor blades have similar fan efficiencies

(5) At high-altitude cruise points with BLI, the pressure ratio of the 24 rotor blades at high flow conditions drops sharply, and the ability to do work is worse compared with models with fewer blades. The pressure ratio of the 18 rotor blades is higher than the pressure ratio of the 15 rotor blades at the same flow rate, and the performance is better. This condition indicates that at high-altitude conditions, the effect of cascade consistency is more pronounced compared with the ground condition and needs to be matched to the blade torsion, inlet parameter conditions

Data Availability

All data included in this study are available upon request by contact with the corresponding author.

Conflicts of Interest

The authors declare that they have no conflicts of interest.

References

[1] R. H. Liebeck, "Design of the blended wing body subsonic transport," *Journal of Aircraft.*, vol. 41, pp. 10–25, 2004.

[2] W. Yan, J. Wu, and Y. Zhagn, "Effects of distributed propulsion crucial variables on aerodynamic performance of blended wing body aircraft," *Journal of Beijing University of Aeronautics and Astronautics.*, vol. 41, pp. 1055–1065, 2015.

[3] A. Ferrar, W. O'Brien, W. Ng, R. Florea, and D. Arend, "Active control of flow in serpentine inlets for blended wing-body aircraft," in *AIAA 2009-4901. 45th AIAA/ASME/SAE/ASEE Joint Propulsion Conference & Exhibit*, Denver, Colorado, USA, 2009.

[4] N. Qin, A. Vavalle, A. Le Moigne, M. Laban, K. Hackett, and P. Weinerfelt, "Aerodynamic considerations of blended wing body aircraft," *Progress in Aerospace Sciences*, vol. 40, no. 6, pp. 321–343, 2004.

[5] Z. Lyu and J. R. R. A. Martins, "RANS-based aerodynamic shape optimization of a blended-wing-body aircraft," in *21st AIAA Computational Fluid Dynamics Conference*, San Diego, CA, USA, 2013.

[6] D. Jung and M. Lowenberg, "Stability and control assessment of a blended-wing-body airliner configuration," in *AIAA Atmospheric Flight Mechanics Conference and Exhibit*, San Francisco, California, USA, 2005.

[7] T. Risch, G. Cosentino, C. Regan, M. Kisska, and N. Princen, "X-48B flight test progress overview," in *47th AIAA Aerospace Sciences Meeting including The New Horizons Forum and Aerospace Exposition*, Orlando, Florida, USA, 2009.

[8] P. Li, B. Zhang, Y. Chen, C. Yuan, and Y. Lin, "Aerodynamic design methodology for blended wing body transport," *Chinese Journal of Aeronautics*, vol. 25, no. 4, pp. 508–516, 2012.

[9] M. B. Carter, R. L. Campbell, O. C. Pendergraft, D. M. Friedman, and L. Serrano, "Designing and testing a blended wing body with boundary-layer ingestion nacelles," *Journal of Aircraft*, vol. 43, no. 5, pp. 1479–1489, 2006.

[10] L. Leifsson, A. Ko, W. H. Mason, J. A. Schetz, B. Grossman, and R. T. Haftka, "Multidisciplinary design optimization of blended-wing-body transport aircraft with distributed propulsion," *Aerospace Science and Technology*, vol. 25, no. 1, pp. 16–28, 2013.

[11] M. A. Sargeant, T. P. Hynes, W. R. Graham, J. I. Hileman, M. Drela, and Z. S. Spakovszky, "Stability of hybrid-wing-body-type aircraft with centerbody leading-edge carving," *Journal of Aircraft*, vol. 47, no. 3, pp. 970–974, 2010.

[12] Z. Zhu, X. Wang, Z. Wu, and Z. Chen, "A new type of transport-blended wing body aircraft," *Acta Aeronautica et Astronautica Sinica*, vol. 29, no. 1, pp. 49–59, 2008.

[13] D. K. Hall, A. C. Huang, A. Uranga, E. M. Greitzer, M. Drela, and S. Sato, "Boundary layer ingestion propulsion benefit for transport aircraft," *Journal of Propulsion and Power*, vol. 33, no. 5, pp. 1118–1129, 2017.

[14] A. S. Gohardani, G. Doulgeris, and R. Singh, "Challenges of future aircraft propulsion: a review of distributed propulsion technology and its potential application for the all electric commercial aircraft," *Progress in Aerospace Sciences*, vol. 47, no. 5, pp. 369–391, 2011.

[15] D. L. Rodriguez, "Multidisciplinary optimization method for designing boundary-layer-ingesting inlets," *Journal of Aircraft*, vol. 46, no. 3, pp. 883–894, 2009.

[16] A. Plas, D. Crichton, M. Sargeant et al., "Performance of a boundary layer ingesting (BLI) propulsion system," in *45th AIAA Aerospace Sciences Meeting and Exhibit*, Reno, Nevada, USA, 2007.

[17] B. J. Lee, M.-S. Liou, and C. Kim, "Optimizing a boundary-layer-ingestion offset inlet by discrete adjoint approach," *AIAA Journal*, vol. 48, no. 9, pp. 2008–2016, 2010.

[18] C. Goldberg, D. Nalianda, D. Mac Manus, P. Pilidis, and J. Felder, "Method for simulating the performance of a boundary layer ingesting propulsion system at design and off-design," *Aerospace Science and Technology*, vol. 78, pp. 312–319, 2018.

[19] N. Budziszewski and J. Friedrichs, *Modelling of a boundary layer ingesting propulsor*, vol. 11, Multidisciplinary Digital Publishing Institute, 2018.

[20] J. Guo, J. Hu, B. Tu, and Z. Wang, "Numerical study of high bypass ratio fan/booster stage with inlet distortion," *Journal of Propulsion Technology*, vol. 40, pp. 2498–2504, 2019.

[21] V. J. Fidalgo, C. A. Hall, and Y. Colin, *A Study of Fan-Distortion Interaction within the NASA Rotor 67 Transonic Stage*, vol. 134, no. 5, 2012Asme Turbo Expo: Power for Land, Sea, & Air, 2012.

[22] H. D. Kim and J. L. Felder, "Control volume analysis of boundary layer ingesting propulsion systems with or without shock wave ahead of the inlet," in *49th AIAA Aerospace Sciences Meeting including the New Horizons Forum and Aerospace Exposition*, Orlando, Florida, USA, 2011.

[23] Y. Elazar and R. P. Shreeve, "Viscous flow in a controlled diffusion compressor cascade with increasing incidence," *Journal of Turbomachinery*, vol. 112, no. 2, pp. 256–265, 1990.